Ultrahigh-Speed Spectral-Domain Optical Coherence Tomography up to 1-MHz A-Scan Rate Using Space–Time-Division Multiplexing

Daewoon Seong, Deokmin Jeon, Ruchire Eranga Wijesinghe, Kibeom Park, Hyeree Kim, Euimin Lee, Mansik Jeon, *Member, IEEE*, and Jeehyun Kim, *Member, IEEE*

***Abstract*— The primary optimization of the imaging speed of optical coherence tomography (OCT) has been keenly studied. In order to overcome the major speed limitation of spectral-domain OCT (SD-OCT), we developed an ultrahigh-speed SD-OCT system, with an A-scan rate of up to 1 MHz, using the method of space–time-division multiplexing (STDM). Multicameras comprising a single spectrometer were implemented in the developed ultrahigh-speed STDM method to eliminate the dead time of operation, whereas STDM was simultaneously employed to enable wide-range scanning measurements at a high speed. By successfully integrating the developed STDM method with GPU parallel processing, 8 vol/s for an image range of 250 × 250 × 2048 pixels (9 × 4.5 × 5 mm) was achieved, with an adjustable volume rate according to the required scanning speed and range. The examined STDM-OCT results of the customized optical thin film confirmed its feasibility for various fields that require rapid and wide-field scanning.**

***Index Terms*— Fourier optical signal processing, parallel processing, space–time-division multiplexing (STDM), spectral-domain optical coherence tomography (OCT), ultrahigh-speed imaging system.**

I. Introduction

OPTICAL coherence tomography (OCT) is a noninvasive and high-resolution imaging technique that enables 2-D imaging and 3-D imaging to measure morphological structures [1], [2]. Due to the method's potential resolution merits, OCT has been widely employed in various applications, such as ophthalmology [3], dentistry [4], [5], otolaryngology [6], [7], dermatology [8], [9], and even industrial fields [10], [11]. In terms of imaging speed, the development of high-speed real-time OCT has been required in order to observe morphological time variation of biological tissues with minimal motion artifacts [12], [13] and to fit a limited inspection time in industrial applications [14], [15].

The imaging speed of the initially developed time-domain OCT (TD-OCT) was limited due to the motor-based scanning mechanism. To overcome this drawback, the Fourier-domain OCT (FD-OCT) was developed to directly obtain depth-resolved spectra without unnecessary movement of mirror and with an improved system sensitivity [16], [17]. Swept-source OCT (SS-OCT) is one of the FD-OCT methods, which has a sufficient imaging speed and detects the spectrum of each wavelength by a photodetector that is mainly influenced by the sweeping rate of the wavelength-tunable light source [18], [19], whereas SS-OCT systems with an MHz high A-scan rate have been presented in previous reports [20]–[22]. Although SS-OCT provides the reduced sensitivity roll-off and high-speed A-scan rate [16], [23], axial resolution is slightly degraded, because of the longer wavelength of the source, and the cost of development is expansive compared to spectral-domain OCT (SD-OCT) [24], [25].

SD-OCT is a widely applied and comparatively economical imaging technique with an exceptional resolution. However, the low speed of the detector has a direct negative impact on the system speed [26]. Thus, multiple attempts were made to enhance the system speed, where those studies are mainly focused on shortening the integration time of the line-scan camera, which needs to sacrifice the detectable maximum number of detector pixels [27]. To further improve the A-line rate, multiple line-scan cameras were used, and their operating times were conversely controlled to use the dead time for capturing [26], [27]. Based on this method, a 1-MHz A-line rate SD-OCT system was developed using four separate cameras [28]. However, the conventional multicamera-based system requires multiple independent spectrometers as much as a number of line-scan cameras, causing inevitable errors of spectrum difference at each spectrometer [26]–[28]. In addition, optical demultiplexer-based FD-OCT, which is used as a spectral analyzer, was introduced to further improve

Manuscript received January 27, 2021; revised March 27, 2021; accepted April 6, 2021. Date of publication April 16, 2021; date of current version May 4, 2021. This work was supported in part by the Bio & Medical Technology Development Program of the NRF funded by the Korean government (the Ministry of Science, ICT and Future Planning) under Grant 2017M3A9E2065282 and in part by the Korea Medical Device Development Fund grant funded by the Korea government (the Ministry of Science and ICT, the Ministry of Trade, Industry and Energy, the Ministry of Health & Welfare, the Ministry of Food and Drug Safety) under Grant KMDF-PR-202009010055, 202011C13. The Associate Editor coordinating the review process was Jing Lei. *(Daewoon Seong and Deokmin Jeon contributed equally to this work.) (Corresponding authors: Mansik Jeon; Jeehyun Kim.)*

Daewoon Seong, Deokmin Jeon, Hyeree Kim, Euimin Lee, Mansik Jeon, and Jeehyun Kim are with the School of Electronic and Electrical Engineering, College of IT Engineering, Kyungpook National University, Daegu 41566, South Korea (e-mail: smc7095@knu.ac.kr; dmjeon@knu.ac.kr; hleeworld@gmail.com; augustmini@knu.ac.kr; msjeon@knu.ac.kr; jeehk@knu.ac.kr).

Ruchire Eranga Wijesinghe is with the Department of Materials and Mechanical Technology, Faculty of Technology, University of Sri Jayewardenepura, Homagama 10200, Sri Lanka (e-mail: erangawijesinghe@sjp.ac.lk).

Kibeom Park is with the Department of Biomedical Engineering, Ulsan National Institute of Science and Technology, Ulsan 44919, South Korea (e-mail: pepl116@unist.ac.kr).

This article has supplementary downloadable material available at https://doi.org/10.1109/TIM.2021.3073701, provided by the authors.

Digital Object Identifier 10.1109/TIM.2021.3073701

the scanning speed up to multi-MHz [29], [30]. Nevertheless, the interference spectrum is diffracted by the limited channels of the demultiplexer, which attenuates the signal and decreases the resolution of frequency interval [29]. Moreover, multiple data acquisition (DAQ) boards and digitizers are required to improve the speed, leading to an increase in the total system prices of optical demultiplexer-based OCT [30].

As an alternative approach to enhancing the speed, the MHz streak-mode OCT, which utilizes an area-scan camera with a resonant scanner in the spectrometer to extend the integration time, was proposed. However, the signal-to-noise ratio (SNR) is much degraded compared with the conventional OCT, whereas nonuniformed exposure of the camera reduces the utilization of the duty cycle as well [31]. In addition, a parallel-OCT-based high-speed system, which improves the illumination power by applying a line focus to the sample, was reported in [32] and [33]. However, the limitations of sensitivity and imaging depth were nonnegligible [32], [34]. Moreover, as an alternative method for improving the scanning rate, multispatial scanning method-based OCT was developed, which utilized wavelength filters to split the beam of the sample arm; however, the axial resolution was reduced because of a higher number of scanning channel [35]. In addition, the space-division multiplexing (SDM) OCT, which illuminates the sample with multiple imaging beams with different optical delays, was also demonstrated [36], [37].

In this study, we developed ultrahigh-speed SD-OCT by optimizing the A-line rate up to 1 MHz, which was achieved by space–time-division multiplexing (STDM). To precisely synchronize the operating time and improve the processing speed, a control software platform was developed using C++ with the Compute Unified Device Architecture (CUDA). The system performance, as an aspect of SDM, was quantitatively evaluated by sensitivity roll-off of each camera, and cross-sectional images were obtained. In addition, the time-division multiplexing (TDM) method, which improves the operating speed and minimizes the alignment error, was verified by the A-scan profiling results of the image-merging process. Moreover, to verify the capability of high-speed STDM-OCT for industrial applications, laboratory-customized subsurface structures of multilayered optical thin films (OTFs) were examined. Therefore, the demonstrated high-speed SD-OCT system has a potential for various applications, where high-speed scanning is essential, such as clinical and biomedical research areas.

II. Materials and Methods

A. Optical Configuration of STDM-OCT

The optical configuration of the STDM-OCT system is illustrated in Fig. 1(a). The light from the broadband light source (SLD-371-HP3, Superlum, Ireland), with a center wavelength of 838 nm, a full-width at half-maximum of 81 nm, and optical power of 27.2 mW, was transmitted to a 50:50 fiber coupler (TW850R5A2, Thorlabs, USA) and evenly distributed to each interferometer. Each interferometer is identically comprised of a 75:25 fiber coupler (TW850R3A2, Thorlabs, USA), a reference arm, and a sample arm. The reference arm consisted of the collimator (F780APC-850, Thorlabs, USA),

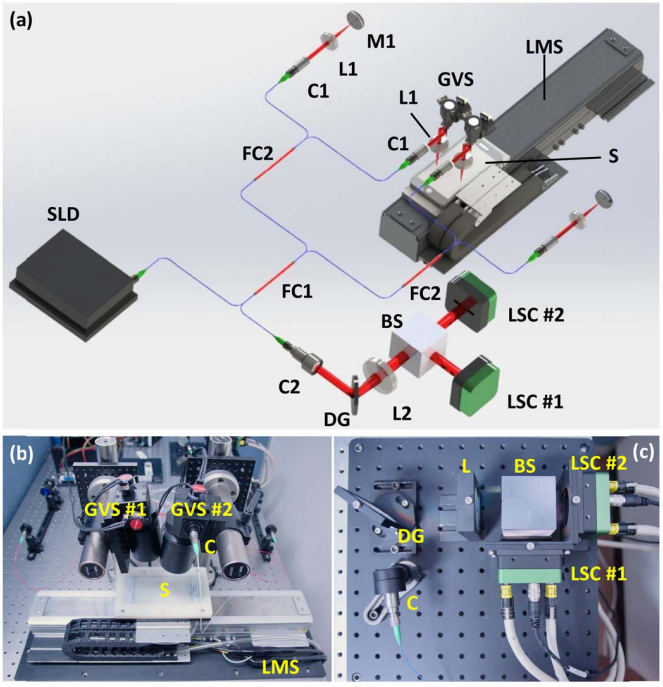

Fig. 1. (a) Optical configuration of the developed STDM-OCT system. (b) Photograph of multiscanners for the implementation of SDM. (c) Photograph of multicameras comprising the single spectrometer for TDM. BS: beam splitter; C: collimator; DG: diffraction grating; FC: fiber coupler; GVS: galvanometer scanner; L: lens; LSC: line-scan camera; LMS: linear-motor stage; M: mirror; S: sample; and SLD: superluminescent diode.

lens (AC508-100-B, Thorlabs, USA), and mirror (PF10-03-P01, Thorlabs, USA). Both the sample and reference arm optics were maintained equivalently, whereas 2-D and 3-D scans were obtained using a galvanometer scanner (GVS002, Thorlabs, USA). In the case of scanning OTF sample, a linear-motor stage (TS-P, YAMAHA, Japan) was used instead of a y-axis galvo scanner to achieve an accurate translation speed for 3-D inspection. To yield an ultrafast A-scan rate, the high-precision SDM method was used, whereas an adequate physical optical path difference between the fiber couplers of each interferometer was accurately regulated. The space-divided coherence signal was generated and properly transmitted to the spectrometer without any distortion. The utilized spectrometer was customized for STDM-OCT, where the conventional spectrometer described in [38] was optically modulated with the addition of beam splitter and additional line-scan camera enabling ultrahigh-speed A-scan rate up to 1 MHz. The diffracted interference signal by diffraction grating (WP-HD1800/840-50.8, Wasatch Photonics, USA) was split up by a beam splitter (BS032, Thorlabs, USA) and separately passed into two line-scan cameras with a resolution of 2048 pixels (e2v OCTOPLUS, TELEDYNE e2v, U.K.), which are the principal components for the application of the TDM technique described in Section II-B. Two frame grabbers (APX-3326A, AVAL DATA, Japan) and a DAQ board (NI PCIe-6363, National Instrument Corporation, USA) were utilized to precisely control the hardware compositions. The photograph of the multiscanners for the implementation of the SDM is presented in Fig. 1(b). In addition, the photograph of

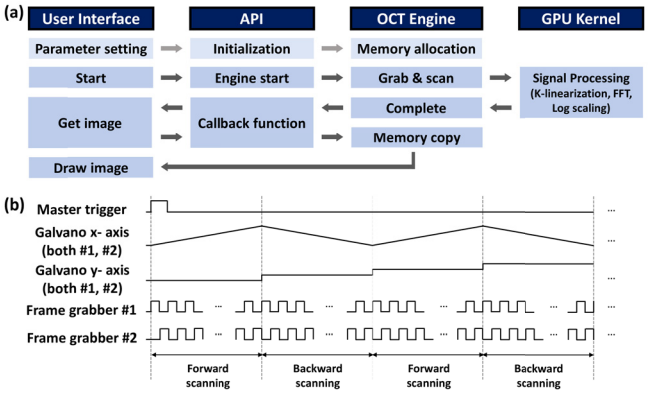

Fig. 2. (a) Software flowchart of STDM-OCT. (b) Timing diagram of synchronized trigger signal sequences. API: application program interface; GPU: graphics processing unit.

a single spectrometer comprised of multicameras, as an aspect of TDM, is presented in Fig. 1(c).

B. Software Flowchart and Overview of System Operation

The developed software algorithm used for STDM-OCT is presented in Fig. 2(a). The developed custom control programming platform is built using C++, CUDA, and Qt. Before the initiation of optical scanning, parameter setting and initialization process, in which the scanning mode was selected and the range was matched to the properties of the sample, were performed. In addition, memories are automatically allocated according to previously initiated values. After the initialization stage, the STDM-OCT engine operation is initiated simultaneously with optical scanning and camera acquisition. The acquired raw signal is transferred to the graphics processing unit (GPU) (from host memory to GPU memory) and processed via the CUDA-based signal processing stage, which includes k-domain linearization, the fast Fourier transform, and log scaling. Through the GPU acceleration, data transmission, processing, and displaying process are properly operated in real-time without buffer overflow. After completing the signal processing of the obtained data in one cycle of x-galvo on GPU, the status of the engine (B-mode completed) is transferred and updated to the user interface (UI) via the callback function in the application programming interface (API). When the UI receives the B-mode completed signal, it starts the "Get image" process by utilizing a callback function in the API for a memory copy of processed data in the OCT engine and displays the image. According to the API-based source code design, precise status synchronization and highly efficient source code management were achieved by loose coupling between the UI and OCT engine.

To control the hardware compositions in order to successfully achieve a 1-MHz A-line rate, synchronization with precise triggering is essentially required. The working sequence is represented by the main trigger, signals of two scanners, and two cameras, as presented in Fig. 2(b). To initiate the starting signal from UI, the DAQ board generates the main trigger, which ensures synchronized timing of the start of implementation. The operations of both scanners and frame grabbers are started simultaneously at the rising edge of the main trigger. To enhance the speed of STDM-OCT, the SDM method, which simultaneously operates the multiscanners, was implemented. Although two sample arms were composed separately, the x-axis and y-axis galvo scanners of each sample arm were controlled similarly with an equal timing by triangular and square waves. Since the raster scanning method was applied to STDM-OCT, the x-axis scanner bidirectionally scans, while the y-axis scanner moves one step in synchronization at the end of each direction (shown in Fig. 2(b) as forward scanning and backward scanning). The path lengths of each scanner were precisely controlled to multiplex the dual scanning data in a single imaging depth. In the case of frame grabbers, identical but reversed trigger sequences of 250 kHz with 50% duty cycle were transferred to each camera to fully utilize the duty cycle without a dead time, which is called TDM in the proposed scheme. Therefore, two continuous A-lines were captured in one period of camera trigger; it guarantees 500 kHz of the effective imaging rate, which is twice faster than the maximum sampling rate of the line-scan camera. These captured A-lines of each camera were alternately composed of B-scan images. Therefore, the speed of STDM-OCT was further increased to 1 MHz by successfully implementing the integrated STDM method.

C. Flowchart for Image Merging Process of STMD-OCT

The image merging process of STDM-OCT with description and generalized configuration of each step is shown in Fig. 3. Since we implemented raster scanning (forward scanning and backward scanning described in Fig. 2 in detail) to fully utilize the duty cycle, the image merging process to obtain the combined B-scan image of each direction is essentially required. As shown in Fig. 3(a) and (b), the B-scan data of both cameras were comprised with both back-and-forth scanning data. We use black for camera #1 and red for camera #2 to distinguish the data of each camera and select representative lines (L1–L4). Fig. 3(c) and (d) demonstrates the merged image of both directions (L1 and L3 for forward and L2 and L4 for backward), and the positions of each line are determined by the description. According to the case of forward scanning presented in Fig. 3(c), the odd-numbered A-lines of merged B-scan images were captured by camera #1 and the even-numbered A-lines by camera #2. As a case of backward scanning shown in Fig. 3(d), a flipping process is additionally required to compensate for the reversed scanning direction of the x-axis scanner after performing the identical merging process of forward scanning. Therefore, the flipping step is applied to Fig. 3(d) and has obtained completed B-scan data, as shown in Fig. 3(e). As an aspect of time-consuming, image merging proceeds in real-time with scanning, data processing, and displaying.

D. Description of Developed UI for Operating the STDM-OCT

Fig. 4 demonstrates the UI of the presented STDM-OCT system. UI was largely divided into two parts: signal displaying [see Fig. 4(a)–(e)] and parameter setting [see Fig. 4(f)]. Fig. 4(a) and (b) shows the real-time cross-sectional OCT image of cameras #1 and #2, respectively. Since SDM was

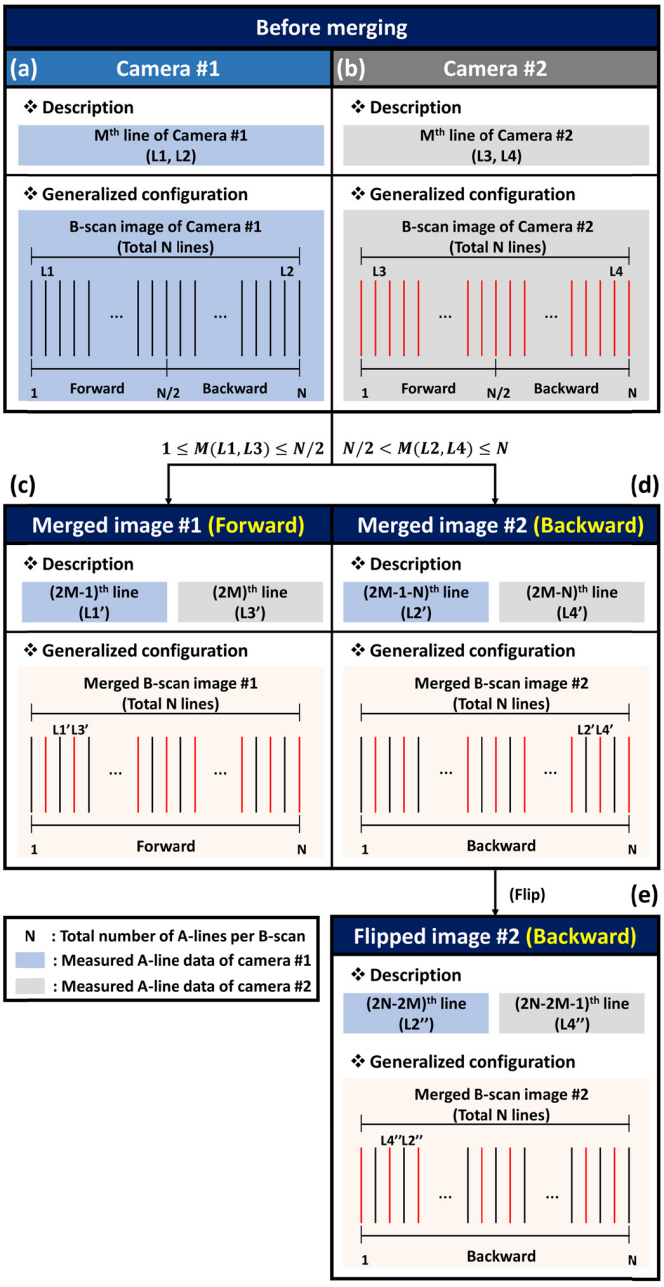

Fig. 3. Detailed description and generalized configuration of flowchart for imaging merging process of STDM-OCT. (a) and (b) Before merging state. (c) and (d) Merged state of (a) and (b). (e) Flipped state of (d).

applied in the presented system, Fig. 4(a) and (b) is composed of the dual signals obtained from two different scanners. Fig. 4(c) and (d) provides the extracted *en face* information of two scanners in real-time measured at different positions according to the preset region of interest in the depth direction. In addition, Fig. 4(e) simultaneously shows the OCT raw signals obtained from both cameras. The operational parameters of the STMD-OCT are demonstrated in Fig. 4(f), which are consisted of the scanning range of both axes, the scanning mode, and the region of interest. The actual operating video of the developed software is shown in Video 1 the Supplementary Material (two-axis galvanometer scanner) and Video 2 in the Supplementary Material (one-axis galvanometer scanner with the linear motor stage).

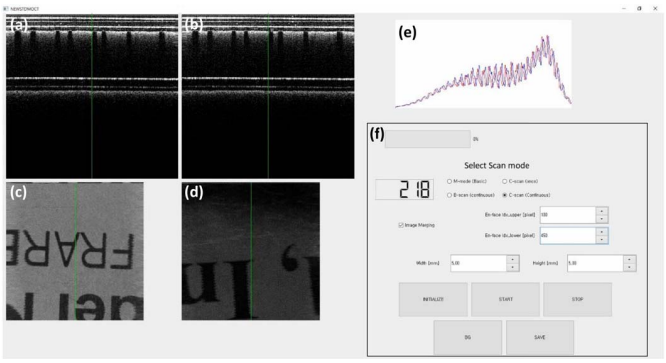

Fig. 4. UI of the STDM-OCT system. (a) OCT cross-sectional view of camera #1. (b) OCT cross-sectional view of camera #2. (c) Extracted *en face* view of scanner #1. (d) Extracted *en face* view of scanner #2. (e) Processed raw signals of both cameras. (f) Parameter setting part for STMD-OCT acquisition.

E. Specification of the Laboratory-Customized OTF Sample

To confirm the feasibility of STDM-OCT for industrial inspection applications, an OTF sample was fabricated. The internal structure of the OTF is largely divided into four layers: a protective film, a transparent film, a deco film, and a base film. The measured thicknesses of each layer were 100, 250, 150, and 100 μm, respectively. Moreover, the measured total thickness of OTF was 700 μm, including the vacuum gaps between each layer, which are 40, 20, and 40 μm. Since the refractive indices of the sublayers in the OTF were different, customized OTF as an industrial sample is appropriate for evaluating the applicability of a high-speed STDM-OCT system. Moreover, the measured total surface area of the sample was 68 $\times$ 140 mm, which is suitable for the inspection of the internal structure using wide-field STDM-OCT.

III. Results

A. Quantitative Evaluation Data of STDM-OCT Performance

To quantitatively analyze the performance of STDM-OCT, we evaluated the presented system as an aspect of SDM and TDM. First, the sensitivity of each camera at a 1-MHz A-line rate was measured at every 100 pixels (0.44-mm interval) in the range of 100th–800th, as presented in Fig. 5(a) and (b). In addition, each value of measured sensitivity was shown in Table I as well. Since the developed single spectrometer consists of two line-scan cameras using a beam splitter to identically divide the coherent signal for each detector, the measured sensitivity roll-off values of the two independently detected signals confirmed the almost equivalent performance. The averaged sensitivity difference between the two cameras is 2.5 dB, and the measured peak sensitivities (at the 100th pixel) were 139 and 137 dB, respectively. To demonstrate the degree of image quality degradation in th depth direction, B-scan images of IR-card were obtained, which are shown in Fig. 5(c) and (d) while varying depth position from the zero-path delay to 2.6 mm. The measured pixel range of B-scan images in the depth direction was distinguished by edge colors (red and blue). Following the edge colors, Fig. 5(c) and (d), which were STDM-OCT images of IR-card, was measured at 0–300 and 300–600, respectively. In addition, we obtained the combined

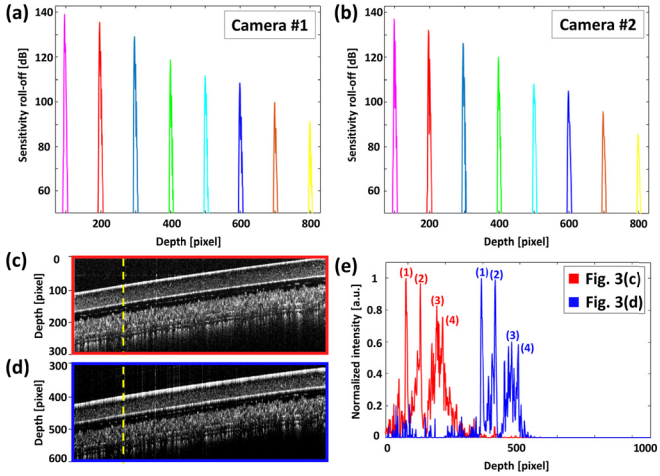

Fig. 5. Quantitative analysis of STDM-OCT performance. (a) Sensitivity fall-off graph of camera #1. (b) Sensitivity fall-off graph of camera #2. (c) and (d) Cross-sectional images of IR-card obtained at different depth positions according to the edge color to evaluate the performance of the SDM. (e) Combined A-scan profile corresponding to the yellow dashed line of Fig. 5(c) and (d).

TABLE I
MEASURED SENSITIVITY ROLL-OFF OF EACH CAMERA

Pixel position	Measured sensitivity [dB]	
	Camera #1	Camera #2
100	139	137
200	135	132
300	129	126
400	118	120
500	111	108
600	108	105
700	99	96
800	91	86

depth-dependent A-scan profile [as presented in Fig. 5(e)], which was extracted from the depth information indicated in the yellow dashed line in Fig. 5(c) and (d). As emphasized in Fig. 5(e), four intensity peaks corresponding to each B-scan image (indicated in red and blue (1)–(4) intensity peaks) were extracted from the yellow dashed line in Fig. 5(c) and (d) for an intensity comparison of cross sections. The averaged intensity of the four blue intensity peaks [depth intensity corresponds to Fig. 5(d)] is 10.6%, which decreased compared with the averaged intensity of the four red intensity peaks [depth intensity corresponds to Fig. 5(c)]. However, the internal sublayers of the IR card were obviously observed in both graphs. These results indicated that the SDM method simultaneously utilizes a full detectable range of camera pixels, which can be applied to the STDM-OCT. Moreover, Table II demonstrates the result of quantitative performance evaluation of the developed STMD-OCT for various categories, including scanning speed, resolution, and imaging depth.

Furthermore, to quantitatively assess the TDM method applied to STDM-OCT, we independently obtained two B-scan images from each camera (before merging) presented in Fig. 6(a) and (b), which are consisted of bidirectional images (demonstrated in Fig. 2(b) as forward scanning and backward scanning). To accurately obtain the scanned data with TDM, the image-merging process described in

TABLE II
OBTAINED QUANTITATIVE PERFORMANCE OF STDM-OCT

Categories of performance evaluation	Obtained value
A-scan rate	1 MHz
Scanning range (representative)	250 × 250 × 2048 pixels (9 × 4.5 × 5 mm)
3D volume rate (representative)	8 vol/s
Sensitivity	139 dB
10 dB roll-off depth	1.3 mm
Lateral resolution	15.6 μm
Axial resolution (in air)	4.4 μm
Imaging depth (in air)	5 mm

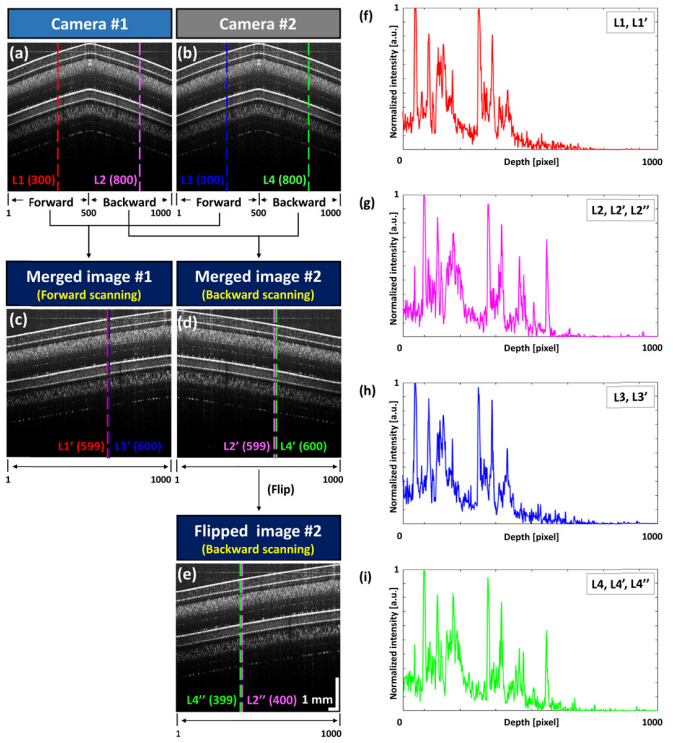

Fig. 6. Verification of the result of image merging process of STMD-OCT, as described in Section II-C. (a) and (b) Cross-sectional IR detection card images of cameras #1 and #2. (c) and (d) Merged images of (a) and (b). (e) Flipped image of (d). (f)–(i) A-scan profiling results of L1 (and L1') to L4 (and L4') indicated in (a)–(d).

Section II-C was essentially required. In order to clearly elucidate the merging process of TDM, four lines (L1–L4) in Fig. 6(a) and (b) were representatively selected. L1 and L3 are the 300th A-lines of the B-scan image, which is part of forward scanning [first to 500th in Fig. 6(a) and (b)] obtained by each camera. L2 and L4 are the 800th A-lines, which were included in backward scanning [500th to 1000th in Fig. 6(a) and (b)]. L1 and L3 (300th) and L2 and L4 (800th) are the same A-line positions of B-scan images, but the obtained structural information is different because cameras were alternatively operated, whereas the galvanometer scanner performed continuous scanning, which can be simultaneously verified by the A-scan profiling results in Fig. 6(e)–(h). Following the image merging process described

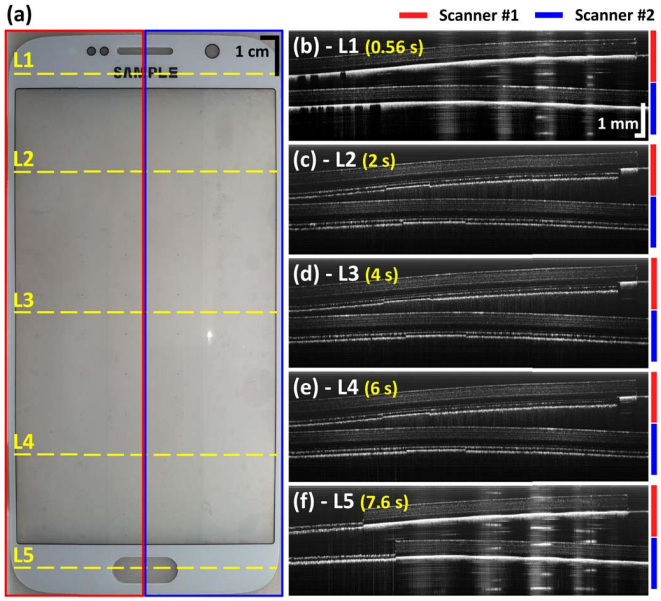

Fig. 7. (a) Top view of the OTF indicated by five yellow dashed lines (L1–L5). (b)–(f) Corresponding cross-sectional OCT images of the OTF samples sequentially measured at five representative lines presented in Fig. 7(a) as L1–L5. Both the red and blue bars, as presented in (b)–(f), represent the space-divided pixel range of each scanner, which covers 0–300 and 300–600, respectively.

in Section II-C, L1 and L3, which are both 300th lines of B-scan images (forward scanning), were matched to L1' (599th) and L3' (600th) in Fig. 6(c), respectively. In addition, the finally obtained B-scan image of backward direction is shown in Fig. 6(e), which is the result of applying the flipping step to Fig. 6(d). In this way, L2 and L4, which are both 800th lines, corresponded to L2' (400th) and L4' (399th) in Fig. 6(d). Hence, these results indicate that the TDM utilizing sequentially operated multicameras in a single spectrometer was accurately implemented to STDM-OCT in order to achieve a 1-MHz A-line sampling rate.

B. High-Speed Inspection System of OTF Using STDM-OCT

To demonstrate the applicability of STDM-OCT for industrial applications, laboratory-customized OTF was initially evaluated as a representative sample of industrial applications. Fabricated OTF sample was placed on a linear-motor stage, and we continued with the 2000 frames of B-scan with 70-μm intervals in the OTF inspection (totally, 2000 $\times$ 2000 $\times$ 2048 pixels), which consumes 8 s for the whole-range scanning of the sample. The obtained results of the OTF inspection through STDM-OCT are presented in Fig. 7. A photograph of the OTF is presented in Fig. 7(a), indicating five representative scanning positions (L1–L5). Moreover, the cross section extracted locations were 140th, 500th, 1000th, 1500th, and 1900th lines, which were measured at 0.56, 2, 4, 6, and 7.6 s, respectively. Cross-sectional images of the OTF measured by STDM-OCT-based inspection system from L1 to L5 are sequentially presented in Fig. 7(b)–(f). In addition, the scanning ranges of each scanner used for SDM are indicated by edge color and color bar (red and blue) in Fig. 7(a). As presented in Fig. 7(b)–(f), the layer structure of the OTF is well distinguished at every measuring position (L1–L5) during the whole-range scanning of the sample. Therefore, these results reveal that the STDM-OCT with a 1-MHz A-line rate is feasible for industrial applications, ensuring high accuracy and reliable quality with a minimum inspection time.

IV. Discussion

Here, we demonstrated the SD-OCT of a 1-MHz A-line rate and introduced a single-spectrometer-based STDM method. Various approaches to enhance imaging speed have been keenly studied and demonstrated. Compared with the conventional method of using a multiple-camera-based system [28], the proposed STDM-OCT of the current research not only resolves the alignment difference error of each spectrometer but also minimizes power loss and effectively economizes the total cost of the system (single-spectrometer-based system configuration). Furthermore, STDM-OCT partially provides enhanced SNR, sensitivity (more than 130 dB), and imaging depth (more than 4 mm) with cost-effective development in comparison with the optical demultiplexer-based method [29], [30], the streak-mode OCT [31], and the parallel OCT [32], [34]. In addition, as an aspect of system price, which is a factor to broaden applications of OCT, SD-OCT has obvious merit compared to SS-OCT. Based on this fact, the developed STDM-OCT provides a 1-MHz A-scan rate, which reduces the inspection time, with comparably low cost to develop compared to SS-OCT. Furthermore, SS-OCT provides a high-speed A-scan rate; however, to the best of our knowledge, the maximum sweeping rate of the commercial swept source is up to 400 kHz, which can be sufficiently obtained by the developed STDM-OCT.

In the case of the SDM method applied to STDM-OCT, two scanners were separately used, where the path lengths were differently maintained to ensure a wide scanning range of the OTF sample. However, single-scanner-based conventional SDM can also be applied to match the sample properties. As an aspect of 3-D volumetric imaging by integrating GPU parallel processing with the STDM method, 8 vol/s for 250 $\times$ 250 $\times$ 2048 pixels (9 $\times$ 4.5 $\times$ 5 mm) was achieved, which covers a much wider scanning range maintaining a high speed compared with the conventional real-time SD-OCT systems [39]–[41]. Furthermore, the volume rate of STDM-OCT can be freely adjusted according to experimental conditions, such as 2 vol/s for 16 $\times$ 8 $\times$ 5 mm and 0.5 vol/s for 30 $\times$ 16 $\times$ 5 mm. In addition, the scanning speed and range can be further increased by applying a multiple-STDM method, which employs additional scanners and cameras. Since we applied GPU acceleration, signal processing and displaying (including cross-sectional images and extracted each scanner's *en face* images) are processed in real time. Only when the image save process is proceeded, displaying B-scan images are updated with preset interval, as shown in Video 2 in the Supplementary Material, while signal processing and saving are processed in real time. In addition, each scanner's spliced B-scan images can be obtained by applying our extracting method described in [42].

Here, a customized OTF was chosen as a sample to confirm the feasibility of the presented ultrahigh-speed OCT system

in industrial applications for the measurement of the final product to inspect the cracks, which causes huge losses and damage to the product. As an aspect of the thickness of the sample, the path length of the reference arm is adjustable to match the focal point without overlapping each scanner's pixel position. Based on the obtained results, STDM-OCT demonstrates the possibility of applying to various fields, which requires high-speed systems, including industrial product manufacturing and inspecting, such as ultrathin glass ($\sim$100 μm), polarizer ($\sim$300 μm), glass substrate ($\sim$500 μm), OTF ($\sim$700 μm), and light guide plate ($\sim$1 mm), which are within an imaging range of the proposed system (4.4 mm) and even biomedical applications. Furthermore, the successful utilization of higher-speed data-transferring techniques and processing techniques and faster line-scan cameras can further enhance the speed of the system beyond the developed 1-MHz A-scan rate.

V. Conclusion

In conclusion, the ultrahigh-speed SD-OCT system up to a 1-MHz A-scan rate was achieved by implementing the developed STDM method. We used multicameras in single spectrometer to resolve the existing limitations of the TDM method, such as alignment errors of each spectrometer, power loss of detected interference signal caused by the use of multiple couplers, and sacrificing the spectral resolution of the camera. In addition, multiscanners were simultaneously used to implement the SDM to cover a wide scanning range. To accurately and rapidly control the hardware operation timing while employing scanners and cameras with high performance, a C++-based software platform with CUDA and Qt was developed and utilized to improve the data processing speed. The quantitatively analyzed results successfully demonstrate the effective implementation of the STDM method for achieving a 1-MHz A-scan rate. In addition, we inspected the OTF as a sample to confirm the feasibility of the developed STDM-OCT system for industrial applications. The obtained results of the implemented STDM method demonstrate the feasibility of the presented system for both real-time volumetric imaging and wide-field scanning at a fast speed according to the required conditions. Hence, the proposed ultrahigh-speed STDM-OCT shows promising results encouraging the application of SD-OCT to various fields, including biomedical and industrial measurement fields, such as the noninvasive quality test of the final product and defect inspection, essentially requiring fast scanning speed, while maintaining the advantages of the conventional SD-OCT system.

References

[1] D. Huang *et al.*, "Optical coherence tomography," *Science*, vol. 254, no. 5035, pp. 1178–1181, 1991.

[2] J. M. Schmitt, "Optical coherence tomography (OCT): A review," *IEEE J. Sel. Topics Quantum Electron.*, vol. 5, no. 4, pp. 1205–1215, Jul. 1999.

[3] W. Drexler, U. Morgner, R. K. Ghanta, F. X. Kärtner, J. S. Schuman, and J. G. Fujimoto, "Ultrahigh-resolution ophthalmic optical coherence tomography," *Nature Med.*, vol. 7, no. 4, pp. 502–507, 2001.

[4] Y. S. Hsieh *et al.*, "Dental optical coherence tomography," *Sensors*, vol. 13, no. 7, pp. 8928–8949, Jul. 2013.

[5] J. Lee *et al.*, "Decalcification using ethylenediaminetetraacetic acid for clear microstructure imaging of cochlea through optical coherence tomography," *J. Biomed. Opt.*, vol. 21, no. 8, Mar. 2016, Art. no. 081204.

[6] S. Van der Jeught, J. J. J. Dirckx, J. R. M. Aerts, A. Bradu, A. G. Podoleanu, and J. A. N. Buytaert, "Full-field thickness distribution of human tympanic membrane obtained with optical coherence tomography," *J. Assoc. Res. Otolaryngol.*, vol. 14, no. 4, pp. 483–494, Aug. 2013.

[7] D. Seong *et al.*, "*In situ* characterization of micro-vibration in natural latex membrane resembling tympanic membrane functionally using optical Doppler tomography," *Sensors*, vol. 20, no. 1, p. 64, Dec. 2019.

[8] F. Liu *et al.*, "A flexible touch-based fingerprint acquisition device and a benchmark database using optical coherence tomography," *IEEE Trans. Instrum. Meas.*, vol. 69, no. 9, pp. 6518–6529, Sep. 2020.

[9] H. Sun *et al.*, "Synchronous fingerprint acquisition system based on total internal reflection and optical coherence tomography," *IEEE Trans. Instrum. Meas.*, vol. 69, no. 10, pp. 8452–8465, Oct. 2020.

[10] M. D. Duncan, M. Bashkansky, and J. Reintjes, "Subsurface defect detection in materials using optical coherence tomography," *Opt. Exp.*, vol. 2, pp. 540–545, Jun. 1998.

[11] Z. Chen, Y. Shen, W. Bao, P. Li, X. Wang, and Z. Ding, "Identification of surface defects on glass by parallel spectral domain optical coherence tomography," *Opt. Exp.*, vol. 23, no. 18, pp. 23634–23646, 2015.

[12] A. F. Low, G. J. Tearney, B. E. Bouma, and I.-K. Jang, "Technology insight: Optical coherence tomography—Current status and future development," *Nature Clin. Pract. Cardiovascular Med.*, vol. 3, no. 3, pp. 154–162, Mar. 2006.

[13] M. Gargesha, M. W. Jenkins, D. L. Wilson, and A. M. Rollins, "High temporal resolution OCT using image-based retrospective gating," *Opt. Exp.*, vol. 17, pp. 10786–10799, Jun. 2009.

[14] M. Bashkansky, M. Duncan, M. Kahn, D. Lewis, and J. Reintjes, "Subsurface defect detection in ceramics by high-speed high-resolution optical coherent tomography," *Opt. Lett.*, vol. 22, pp. 61–63, Jan. 1997.

[15] N. H. Cho, K. Park, J.-Y. Kim, Y. Jung, and J. Kim, "Quantitative assessment of touch-screen panel by nondestructive inspection with three-dimensional real-time display optical coherence tomography," *Opt. Lasers Eng.*, vol. 68, pp. 50–57, May 2015.

[16] M. A. Choma, M. V. Sarunic, C. Yang, and J. A. Izatt, "Sensitivity advantage of swept source and Fourier domain optical coherence tomography," *Opt. Exp.*, vol. 11, no. 18, pp. 2183–2189, 2003.

[17] R. Leitgeb, C. K. Hitzenberger, and A. F. Fercher, "Performance of Fourier domain vs. time domain optical coherence tomography," *Opt. Exp.*, vol. 11, no. 8, pp. 889–894, Apr. 2003.

[18] S. Chinn, E. Swanson, and J. Fujimoto, "Optical coherence tomography using a frequency-tunable optical source," *Opt. Lett.*, vol. 22, pp. 340–342, Mar. 1997.

[19] T. Klein and R. Huber, "High-speed OCT light sources and systems," *Biomed. Opt. Exp.*, vol. 8, pp. 828–859, Feb. 2017.

[20] T. Klein, W. Wieser, C. M. Eigenwillig, B. R. Biedermann, and R. Huber, "Megahertz OCT for ultrawide-field retinal imaging with a 1050 nm Fourier domain mode-locked laser," *Opt. Exp.*, vol. 19, pp. 3044–3062, Feb. 2011.

[21] T. Klein, W. Wieser, L. Reznicek, A. Neubauer, A. Kampik, and R. Huber, "Multi-MHz retinal OCT," *Biomed. Opt. Exp.*, vol. 4, pp. 1890–1908, Oct. 2013.

[22] J. P. Kolb, T. Pfeiffer, M. Eibl, H. Hakert, and R. Huber, "High-resolution retinal swept source optical coherence tomography with an ultra-wideband Fourier-domain mode-locked laser at MHz A-scan rates," *Biomed. Opt. Exp.*, vol. 9, pp. 120–130, Jan. 2018.

[23] F. Lavinsky and D. Lavinsky, "Novel perspectives on swept-source optical coherence tomography," *Int. J. Retina Vitreous*, vol. 2, no. 1, pp. 1–11, Dec. 2016.

[24] B. Potsaid *et al.*, "Ultrahigh speed 1050nm swept source/Fourier domain OCT retinal and anterior segment imaging at 100,000 to 400,000 axial scans per second," *Opt. Exp.*, vol. 18, pp. 20029–20048, Sep. 2010.

[25] A. Y. Alibhai, C. Or, and A. J. Witkin, "Swept source optical coherence tomography: A review," *Current Ophthalmol. Rep.*, vol. 6, pp. 7–16, Mar. 2018.

[26] L. An, G. Guan, and R. K. Wang, "High-speed 1310 nm-band spectral domain optical coherence tomography at 184,000 lines per second," *J. Biomed. Opt.*, vol. 16, no. 6, 2011, Art. no. 060506.

[27] L. An, P. Li, T. T. Shen, and R. Wang, "High speed spectral domain optical coherence tomography for retinal imaging at 500,000 A-lines per second," *Biomed. Opt. Exp.*, vol. 2, pp. 2770–2783, Oct. 2011.

[28] O. P. Kocaoglu, T. L. Turner, Z. Liu, and D. T. Miller, "Adaptive optics optical coherence tomography at 1 MHz," *Biomed. Opt. Exp.*, vol. 5, pp. 4186–4200, Dec. 2014.

[29] K. Ohbayashi *et al.*, "60 MHz A-line rate ultra-high speed Fourier-domain optical coherence tomography," in *Proc. 12th Coherence Domain Opt. Methods Opt. Coherence Tomogr. Biomed.*, Feb. 2008, Art. no. 68470M.
[30] D.-H. Choi, H. Hiro-Oka, K. Shimizu, and K. Ohbayashi, "Spectral domain optical coherence tomography of multi-MHz A-scan rates at 1310 nm range and real-time 4D-display up to 41 volumes/second," *Biomed. Opt. Exp.*, vol. 3, pp. 3067–3086, Dec. 2012.
[31] R. Wang, J. X. Yun, X. Yuan, R. Goodwin, R. R. Markwald, and B. Z. Gao, "Megahertz streak-mode Fourier domain optical coherence tomography," *J. Biomed. Opt.*, vol. 16, no. 6, 2011, Art. no. 066016.
[32] J. Barrick, A. Doblas, M. R. Gardner, P. R. Sears, L. E. Ostrowski, and A. L. Oldenburg, "High-speed and high-sensitivity parallel spectral-domain optical coherence tomography using a supercontinuum light source," *Opt. Lett.*, vol. 41, pp. 5620–5623, Dec. 2016.
[33] B. Fang *et al.*, "Full-range line-field optical coherence tomography for high-accuracy measurements of optical lens," *IEEE Trans. Instrum. Meas.*, vol. 69, no. 9, pp. 7180–7190, Sep. 2020.
[34] K.-S. Lee *et al.*, "High speed parallel spectral-domain OCT using spectrally encoded line-field illumination," *Appl. Phys. Lett.*, vol. 112, no. 4, Jan. 2018, Art. no. 041102.
[35] T. Mekonnen, A. Kourmatzis, J. Amatoury, and S. Cheng, "Simultaneous multi-spatial scanning optical coherence tomography (OCT) based on spectrum-slicing of a broadband source," *Meas. Sci. Technol.*, vol. 30, no. 4, Feb. 2019, Art. no. 045203.
[36] C. Zhou, A. Alex, J. Rasakanthan, and Y. Ma, "Space-division multiplexing optical coherence tomography," *Opt. Exp.*, vol. 21, pp. 19219–19227, Aug. 2013.
[37] Y. Huang, M. Badar, A. Nitkowski, A. Weinroth, N. Tansu, and C. Zhou, "Wide-field high-speed space-division multiplexing optical coherence tomography using an integrated photonic device," *Biomed. Opt. Exp.*, vol. 8, pp. 3856–3867, Aug. 2017.
[38] D. Seong *et al.*, "Dynamic compensation of path length difference in optical coherence tomography by an automatic temperature control system of optical fiber," *IEEE Access*, vol. 8, pp. 77501–77510, 2020.
[39] M. Sylwestrzak, M. Szkulmowski, D. Szlag, and P. Targowski, "Real-time imaging for spectral optical coherence tomography with massively parallel data processing," *Photon. Lett. Poland*, vol. 2, no. 3, pp. 137–139, Oct. 2010.
[40] K. Zhang and J. U. Kang, "Real-time 4D signal processing and visualization using graphics processing unit on a regular nonlinear-k Fourier-domain OCT system," *Opt. Exp.*, vol. 18, no. 11, pp. 11772–11784, 2010.
[41] K. Zhang and J. U. Kang, "Real-time intraoperative 4D full-range FD-OCT based on the dual graphics processing units architecture for microsurgery guidance," *Biomed. Opt. Exp.*, vol. 2, pp. 764–770, Apr. 2011.
[42] S. A. Saleah *et al.*, "Integrated quad-scanner strategy-based optical coherence tomography for the whole-directional volumetric imaging of a sample," *Sensors*, vol. 21, no. 4, p. 1305, Feb. 2021.

Daewoon Seong received the B.E. degree from the School of Electronics Engineering, Kyungpook National University, Daegu, Republic of Korea, in 2020.

He is currently a MD Researcher with the School of Electronic and Electrical Engineering, Kyungpook National University. His research focuses on developing high-speed and high-resolution optical imaging systems, photoacoustic microscopy, and optical coherence tomography applied to medical fields and industrial applications.

Deokmin Jeon received the Ph.D. degree in electronics engineering from Kyungpook National University, Daegu, South Korea, in 2020.

He is currently with Samsung Electronics Company Ltd., Republic of Korea. His research interests include the development of biomedical and industrial imaging techniques, including optical coherence tomography, parallel computing, and 3-D vision technology.

Ruchire Eranga Wijesinghe received the B.Sc. and Ph.D. degrees in electronics engineering from Kyungpook National University, Daegu, South Korea, in 2012 and 2018, respectively.

He is currently a Senior Lecturer with the Department of Materials and Mechanical Technology, University of Sri Jayewardenepura, Homagama, Sri Lanka. His research interests are in the development of high-resolution novel biological and biomedical imaging techniques, including optical coherence tomography and microscopy for clinical utility.

Kibeom Park received the B.Sc. and Ph.D. degrees in electronics engineering from Kyungpook National University, Daegu, South Korea, in 2012 and 2018, respectively.

He is currently a Post-Doctoral Researcher with the Department of Department of Biomedical Engineering, Ulsan National Institute of Science and Technology, Ulsan, South Korea. His research interests are in the development of high-throughput optical imaging techniques in biomedical and industrial fields.

Hyeree Kim received the B.E. degree in avionic electronics engineering from Kyungwoon University, Gumi, Republic of Korea, in 2018.

She is currently an MS Researcher with the Electronics Engineering Department, Kyungpook National University, Daegu, South Korea. Her research interests are the development of biomedical imaging systems, including optical coherence tomography and optical instrument optimization design.

Euimin Lee received the B.E. degree from the School of Electronic and Electrical Engineering, Kyungpook National University, Daegu, Republic of Korea, in 2020.

He is currently a MD Researcher with the School of Electronics Engineering, Kyungpook National University. His research focuses on development of imaging processing technique and convolutional neural networks using optical coherence tomography applied to industrial and agricultural application.

Mansik Jeon (Member, IEEE) received the Ph.D. degree in electronics engineering from Kyungpook National University, Daegu, Republic of Korea, in 2011.

He is currently an Associate Professor with the School of Electronics Engineering, Kyungpook National University. His research interests are in the development of nonionizing and noninvasive novel biomedical imaging techniques, including photoacoustic tomography, photoacoustic microscopy, optical coherence tomography, ultrasonic imaging, handheld scanner, and their clinical applications.

Jeehyun Kim (Member, IEEE) received the Ph.D. degree in biomedical engineering from The University of Texas at Austin, Austin, TX, USA, in 2004.

He has worked as a Post-Doctoral Researcher at the Beckman Laser Institute, University of California at Irvine, Irvine, CA, USA. He is currently an Associate Professor with Kyungpook National University, Daegu, Republic of Korea. His research interests are in biomedical imaging and sensing, neuroscience studies using multiphoton microscopy, photoacoustic imaging, and other novel applications of sensors.